Nuclear Inst. and Methods in Physics Research B 437 (2018) 1–7

Contents lists available at ScienceDirect

Nuclear Inst. and Methods in Physics Research B

journal homepage: www.elsevier.com/locate/nimb

Systematic analysis of different experimental approaches to measure electronic stopping of very slow hydrogen ions

D. Roth[a], C.E. Celedon[a,b,c], D. Goebl[a], E.A. Sanchez[b], B. Bruckner[a], R. Steinberger[d], J. Guimpel[b], N.R. Arista[b], P. Bauer[a,*]

[a] Johannes-Kepler Universität Linz, IEP-AOP, Altenbergerstraße 69, A-4040 Linz, Austria
[b] Centro Atómico Bariloche and Instituto Balseiro, San Carlos de Bariloche, Argentina
[c] Laboratorio de Colisiones Atómicas, Departamento de Física, UTFSM, Valparaíso, Chile
[d] Christian Doppler Laboratory for Microscopic and Spectroscopic Material Characterization, Zentrum für Oberflächen- und Nanoanalytik (ZONA), Johannes-Kepler Universität Linz, Altenbergerstraße 69, A-4040 Linz, Austria

ARTICLE INFO

Keywords:
LEIS
Electronic stopping
Protons
Nickel
Transmission
Backscattering

ABSTRACT

The electronic stopping cross section (SCS) of Ni for slow H^+, $H_2{}^+$, D^+ and $D_2{}^+$ ions has been investigated for different types of targets in two complementary experimental geometries, i.e., in transmission and backscattering. To warrant sample purity, both a high purity nickel sheet and nanometer Ni layers were prepared in-situ under ultra-high-vacuum conditions. In an alternative approach, ultra-thin samples were prepared ex-situ as self-supporting foils and as nanometer films on a polished substrate (silicon). Identical SCS results are obtained in backscattering using the in-situ prepared film and the high purity sheet. The ex-situ prepared targets contained considerable concentrations of impurities of low atomic numbers, whose contribution to the SCS can be rectified by applying Bragg's rule using TRIM stopping for the impurities. In this way for the ex-situ targets the accuracy of the resulting SCS data is improved considerably. Concordant stopping cross section data are obtained in both geometries. The achieved accuracy does, however, not permit to spot a possible influence of different impact parameter regimes explored in transmission and in backscattering geometries.

1. Introduction

Ions propagating in solids are slowed down due to interaction with both, nuclei and electrons, i.e. by nuclear and electronic stopping, respectively. The mean energy loss per path length is given by the stopping power $S = \mathrm{d}E/\mathrm{d}x$. In other words, S is the deceleration force acting on the ion. When interactions of ions with atoms or molecules are investigated, the stopping cross section $\varepsilon = S/N$ is a useful quantity, where n stands for the atomic or molecular density of the target material. Profound understanding of the underlying physical processes as well as accurate experimental data are required in many different fields, e.g., space weathering [1], nuclear fusion research [2], and materials research (ion implantation, ion beam analysis) [3,4].

At high ion velocities $v \gg v_F$ (v_F denotes the Fermi velocity of the target electrons), energy dissipation of the projectile is mainly due to electronic stopping and accurate theoretical models are available [5–9]. At low ion velocities $v < v_F$, electronic stopping is due to interaction with the valence electrons; also nuclear stopping may contribute considerably to the total energy loss. The presence of the slow ion in the target material represents a strong perturbation in the states of valence and conduction electrons. Consequently, any theoretical description of electronic stopping of slow ions constitutes a complex many-body problem. Hence, the physics of electronic interactions of slow ions with solids is still a subject of current research [10–12].

Also from an experimental point of view it is demanding to obtain accurate stopping data for slow ions: in recent years, SCS acquired by complementary experimental techniques (transmission and backscattering) exhibited rather pronounced differences in some cases (e.g., Cu and Ag, [13–15]) while for others concordant results were reported (e.g., Al and Au, [16,17,13,18]). The observed differences might point towards a systematic influence of the experimental geometry, due to different impact parameter selection in transmission and in backscattering. This point has recently been discussed thoroughly by Sigmund and Schinner [19].

In order to scrutinize what are the possible reasons for the observed differences between low-energy transmission and backscattering experiments, a cooperation has been started between the Centro Atómico Bariloche and the Johannes-Kepler-Universität Linz (JKU). In a similar

* Corresponding author.
E-mail address: peter.bauer@jku.at (P. Bauer).

https://doi.org/10.1016/j.nimb.2018.09.028
Received 6 April 2017; Received in revised form 7 September 2018; Accepted 21 September 2018
Available online 18 October 2018
0168-583X/ © 2018 The Authors. Published by Elsevier B.V. This is an open access article under the CC BY license (http://creativecommons.org/licenses/BY/4.0/).

cooperation, Mertens et al. showed that around the stopping maximum consistent stopping data could be obtained by transmission and by backscattering measurements, when the influence of surface contaminations was properly taken into account for the foils used in transmission measurements [20]. In this study, the electronic stopping of slow H ions in Ni was chosen as benchmark test. As a transition metal, Ni is interesting from a physical point of view, but it is also chemically reactive and therefore provides information on the relevance of target impurities of low atomic numbers (low Z impurities, e.g., carbon, oxygen).

With the aim of achieving accurate electronic stopping cross section data, systematic errors had to be minimized in target preparation as well as in energy loss measurements, both in transmission and in backscattering geometry.

The paper is structured as follows: in Section 2, theoretical models to describe electronic stopping of slow ions are discussed briefly, followed by Section 3, in which simulation programs used in data evaluation of transmission and backscattering experiments are presented. In Section 4, both experimental approaches as well as the techniques used for sample production and characterization are explained in detail. The experimental results are presented and discussed in Section 5.

2. Theory

Since at low ion energies, electronic stopping is due to the excitation of conduction/valence electrons, Ni ([Ar]$3d^8 4s^2$) exhibits an interesting electronic density of states (DOS), with a high DOS at energies below the Fermi level, E_F [21]. In this velocity regime, it has been shown that for a Free Electron Gas (FEG) the stopping power is proportional to the ion velocity, $dE/dx = Q{\cdot}v$ [22]. The friction coefficient, Q, of an ion of atomic number Z_1 in a FEG has been determined in a nonlinear model within the Density Functional Theory (DFT) framework [23,24], resulting in $Q = n_e{\cdot}m_e{\cdot}v_F{\cdot}\sigma_{tr}$, with the electronic density n_e, and the transport cross section σ_{tr}. This description considers the conduction electrons of a metal as a FEG with a density-related r_s parameter, $r_s = (3/4\pi n_e)^{1/3}$; the Fermi velocity is given by $v_F = 1.919/r_s$. It has been shown empirically that the nonlinear DFT model [23] successfully describes experimental stopping data for protons at $v \leq v_F$ for a wide range of materials, when effective r_s values (deduced from plasmon energies) are used [25]. For the present work we have employed the DFT results for $Q(r_s)$ from Ref. [26].

3. Simulations

The large scattering cross sections at low ion energies lead to an increasing probability for multiple scattering and, consequently, to an increase of nuclear stopping and the path length inside the target, respectively [27]. Therefore, evaluation of data from both, transmission and backscattering experiments needs to rely on Monte Carlo (MC) simulations which allow for an adequate consideration of multiple scattering and permit to disentangle contributions from nuclear and electronic stopping, respectively.

Simulations of energy loss spectra acquired in transmission were performed using a MC code, which was employed already in previous investigations [28–30]. These simulations include information on surface roughness of the target foil, stopping forces, intrinsic straggling and a screened scattering potential of Molière type [31], with the aim of analyzing and explaining the main features of the experimental data. The screening length is determined from the analysis of multiple-scattering angular distributions, and the electronic stopping force results from the comparison of the simulations to experimental angular dependent energy loss spectra [28,32].

For the evaluation of backscattering experiments, MC simulations of energy spectra were performed employing the TRBS code [33], which permits to simulate multi-layer targets. In the simulations, for the individual layers electronic stopping (from TRIM85 [34]) and the strength of the scattering potential (ZBL [34] or Molière [31] screening) can be optimized, e.g. following Ref. [35]. A proper choice of these parameters is essential for accurate evaluation of electronic stopping from energy spectra of backscattered ions [36]. When the stopping power is evaluated by comparing the backscattering spectra of the material of interest and of a reference material of similar atomic number, the scattering potential does not introduce any noticeable systematic errors [37]. In this contribution, the ZBL potential without a screening length correction was applied. Details concerning the evaluation procedure are explained in the experimental section.

4. Experiment

4.1. Target preparation and characterization

4.1.1. Transmission foils

The self-supported ultra-thin foils used in the transmission experiments were produced ex-situ by sputter deposition of Ni films on cleaved polished NaCl crystals under high vacuum conditions. After careful dissolution of the salt by deionized water at 49 °C, the foils floating on the surface were transferred to TEM grids. The thickness and the composition of the films were determined by use of twin samples deposited onto SiO_2 and glass, thereby disregarding possible influences of the preparation of the free-standing foils (incorporation of impurities, oxidation).

The geometrical thickness of the films was measured by low-angle X-ray reflectometry (XRR), which evaluates the interference pattern to yield the geometrical thickness of the Ni film; surface contaminations contribute only little due to the lower sensitivity of XRR to low Z surface impurities. This technique is little sensitive to impurities present in the bulk of the films. Therefore, a mean geometrical film thickness is obtained, but the film density due to incorporated impurities has to be determined independently. The investigated surface area is ~1 cm^2 and yields information on film roughness. Possible systematic errors may result from not perfectly plane substrates, too large film roughness, bulk impurities or misalignment. The statistical uncertainty arises from the evaluation of peak positions and depends on the number of visible diffraction orders. Independently, the roughness (including surface contamination) has been checked by Atomic Force Microscopy (AFM). Calibration of the AFM by scanning an MCNC step-height reference of 44 nm under the same experimental conditions as in the present measurements permitted to evaluate the geometrical thicknesses of the films, with an estimated precision of ~5 to 10% (standard deviation).

Depth profiling by means of X-ray photoelectron spectroscopy (XPS) during Ar bombardment yielded information on surface and bulk contaminations, as well as information on the chemical environment of the Ni atoms; the results are presented in Section 5.

4.1.2. Backscattering films

For the backscattering experiments three types of Ni samples were used. First, a set of ultra-thin Ni films was deposited ex-situ by e-beam evaporation on Si under high vacuum conditions. Second, ultra-thin Ni films were deposited in-situ on B/Si using an Omicron EFM-3T evaporation system in ultra-high vacuum (UHV). Note that during evaporation the pressure in the vacuum chamber never exceeded $\sim 2 \times 10^{-10}$ mbar (accomplished by use of a 99.99% Ni rod as evaporation material and two LN_2 cold traps, respectively). Third, a high purity Ni sheet[1] was mechanically polished, cleaned in isopropanol in an ultrasonic bath, and sputter-cleaned by 3 keV Ar^+ ions in the UHV setup. Purity of the in-situ Ni films, the Ni sheet and a reference sample (Cu) was checked by Auger Electron Spectroscopy (AES), the ex-situ Ni films were analyzed by XPS at ZONA (JKU); the XPS results are presented in Section 5.

[1] According to time-of-flight Elastic Recoil Detection (TOF-ERD), performed at Uppsala University, the amount of all bulk impurities was < 1%.

For determination of the film thicknesses in terms of Ni atoms per unit area (areal density), Rutherford Backscattering Spectrometry (RBS) measurements were performed. The RBS analysis averages over an area smaller than ~1 mm^2. The areal densities are determined by comparing the peak areas of Ni to that of a gold reference sample of known areal density, when recorded for the same primary charge. In RBS, neither light surface nor bulk contaminations have any influence on the resulting areal densities. Uncertainties in the stopping power of the reference sample may introduce a systematic error of ± 3% in the film thickness. Statistical uncertainties are due to fluctuations of the primary beam current and due to counting statistics. From the RBS areal densities, the thicknesses of the Ni films were determined by use of the Ni atomic density to 13.9 nm ± 0.4 nm, 14 nm ± 0.3 nm, and 12.8 nm ± 0.5 nm for the ex-situ films; for the in-situ films thicknesses of 9.1 nm ± 0.3 nm, 8.3 nm ± 0.2 nm, and 6.5 nm ± 0.3 nm were obtained. Note that these uncertainties correspond to the statistical errors only.

4.2. Stopping measurements

4.2.1. Energy spectra in transmission

The ion beams were produced by a Colutron hot-cathode ion source [38]. A mass selected and focused ion beam entered a high vacuum collision chamber after deflection by 18° to remove the neutral particles from the beam. After transmission through the Ni foil, the energy spectra (energy loss distributions) of positively charged projectiles were measured using a 127° electrostatic cylindrical energy analyzer with an energy and angular resolution of 2% (FWHM) and 1.8°, respectively. The acquired energy spectra were corrected for the transmission function of the analyzer, the efficiency of the electron multiplier (ETP AEM 1000), and the dependence of the ion fraction on the outgoing projectile energy [32].

Information on electronic stopping is deduced from the energy spectra of particles that impinge under normal incidence and are transmitted in a direction close to perpendicular exit (zero exit angle). The energy lost by a projectile is evaluated as the difference between the incident energy E_0 and the most probable exit energy, E_p, obtained from the corrected spectrum of the transmitted particles. The stopping power can be directly obtained by dividing the energy loss ($E_0 - E_p$) by the foil thickness, and the SCS by dividing the stopping power by the atomic target density. Compared to stopping power measurements in backscattering, one may expect the energy loss measurement in transmission geometry to explore larger impact parameters [19], since in transmission the contributions to the energy loss due to the elastic collisions with target nuclei and due to the path enlargement produced by multiple scattering events are minimized.

In Fig. 1, energy spectra are shown for a direct beam of 3.5 keV D^+, and after transmission through a 15 nm self-supported Ni film, respectively. The primary ion energy and the most probable projectile energy after transmission are indicated with labels E_0 and E_p, respectively. Also shown are the results of corresponding MC-simulations. For the interaction potential the screening length was adjusted to reproduce the normalized angular distributions. Excellent agreement between experiment and simulation is achieved after proper choice of simulation parameters (compare Section 3).

In Fig. 2a, the relative transmitted intensity, $F_{MS}(\theta)/F_{MS}(\theta = 0°)$, is shown as a function of the exit angle θ, for 9 keV H^+ ions. Multiple-scattering functions [39] are depicted as obtained for ZBL, Molière and Thomas-Fermi potentials with screening lengths of $0.9a_{ZBL}$, $0.8a_L$ and $0.84a_{TF}$, respectively [40,41] (solid lines). Here, a_L denotes the Lindhard screening length [42]. Experiment and simulations agree very well. For the MC simulations within this manuscript, the Molière potential was used. In a next step, the foil properties were characterized by means of MC simulations of the angular dependence of the energy loss spectra. In Fig. 2b we present the difference between the energy loss values $\Delta E(\theta)$ and $\Delta E(\theta = 0°)$, as a function of the exit angle. These results were analyzed by using the three-component model proposed in Ref. [43],

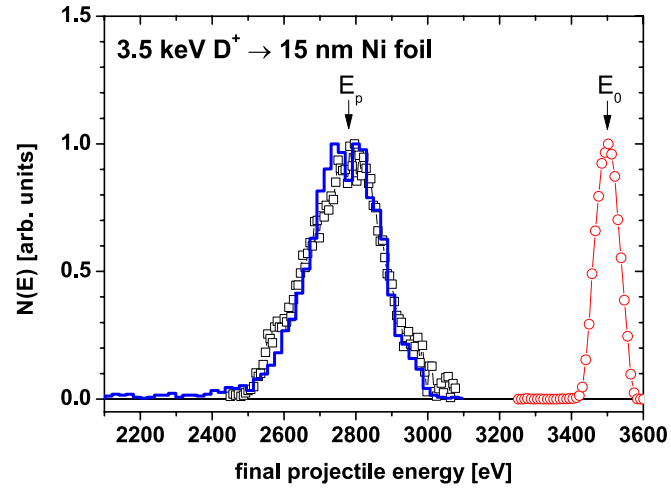

Fig. 1. Energy spectra of a 3.5 keV D^+ direct ion beam (red open circles) and of ions transmitted through a 15 nm self-supported Ni foil (black open squares). The blue solid line corresponds to the Monte Carlo (MC) simulation of the transmitted particles. E_0 and E_p indicate the primary ion energy and the most probable energy after transmission, respectively. (For interpretation of the references to colour in this figure legend, the reader is referred to the web version of this article.)

similarly as for other samples [28,32]. This model permits to separate the contributions to the energy loss from (i) path-length enlargement (dash-dotted line), (ii) elastic energy loss (dash-dot-dotted line), and (iii) foil roughness (dashed line). As a result, the angular dependence of the energy loss is dominated by path-length enlargement and foil roughness, whereas the elastic contribution is found to be small. In the MC simulations, 9% foil roughness was used, in close agreement to the values obtained by XRR (8%) and AFM measurements (10%). As shown in Fig. 2b, both the MC simulations and the three-component model yield very good agreement with the experiment. From the MC simulations a ratio of nuclear to electronic energy loss is obtained, which for protons emerging at zero scattering angle results in 0.5% to 2%, depending on energy: the lower the energy, the larger is the contribution of nuclear stopping. For deuterons, nuclear energy losses contribute nearly twice as much as for protons of the same energy.

4.2.2. Energy spectra in backscattering

The backscattering measurements were performed employing the UHV time-of-flight low energy ion scattering (TOF-LEIS) setup ACOLI-SSA [44]. TOF-LEIS spectra were recorded by use of hydrogen and deuterium ion beams (monomers and dimers) in the range of 0.33 keV/u–10 keV/u (scattering angle $\theta = 129°$) and were converted to energy spectra following standard procedures. The electronic SCS data of Ni, ε_{Ni}, are evaluated following two different experimental approaches: first, for nanometer films ε_{Ni} are determined from the widths of the peaks due to scattering from Ni. The electronic SCS values of Ni are obtained by use of TRBS simulations, in which the film areal densities as determined by RBS are used and ε_{Ni} is optimized as the only free parameter to reproduce the shape of the experimental spectrum. In Fig. 3, experimental and simulated spectra of 6 keV D_2^+ scattered from an 8.3 nm Ni film on B/Si are shown as a function of energy. Excellent agreement between experiment and simulation is achieved for proper choice of ε_{Ni} (referred to in Fig. 3 as ε_{best}). Note that the simulated spectrum has been convoluted with a Gaussian to account for experimental resolution. In order to show the sensitivity of this procedure, additional simulations are displayed where ε_{best} was varied by ± 10%. A variation of the film thickness.

Second, ε_{Ni} is deduced from energy spectra recorded for the same primary charge for projectiles backscattered from the Ni sheet and from a reference sample of known SCS, ε_{ref} (Cu). In this approach, ε_{Ni} is

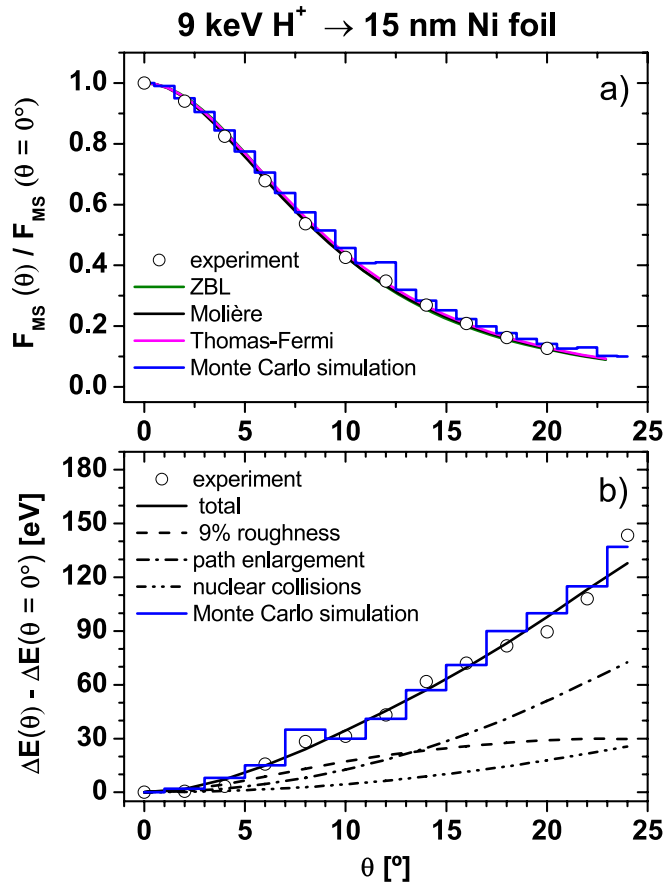

Fig.2. (a) Normalized angular distribution of 9 keV H^+ transmitted through a 15 nm Ni foil. The lines show the multiple-scattering distribution calculated using different potentials (ZBL, Molière and Thomas-Fermi). The blue step line is the result of the MC simulations. (b) Angular dependence of the energy loss referred to the energy loss in the forward direction ($\theta = 0°$). The dashed line shows the effects of foil roughness, the dash-dotted the contribution of path-length enlargement, and the dash-dot-dotted the contribution of the elastic scattering obtained from the three-component model [43]. The result of the MC simulation is presented in blue. (For interpretation of the references to colour in this figure legend, the reader is referred to the web version of this article.)

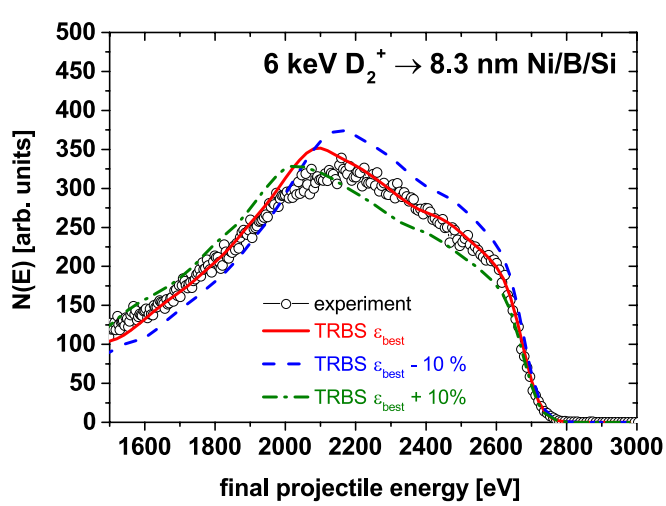

Fig. 3. Experimental TOF-LEIS backscattering spectra of 6 keV D_2^+ ions measured on Ni deposited on B/Si substrates. Also shown the results of TRBS simulations: as a solid line—spectrum with optimized Ni SCS $\varepsilon_{best} = 3.87 \times 10^{-15}$ eV cm^2/atom, as dash-dotted and dashed lines—spectra for $\varepsilon_{best} \pm 10\%$.

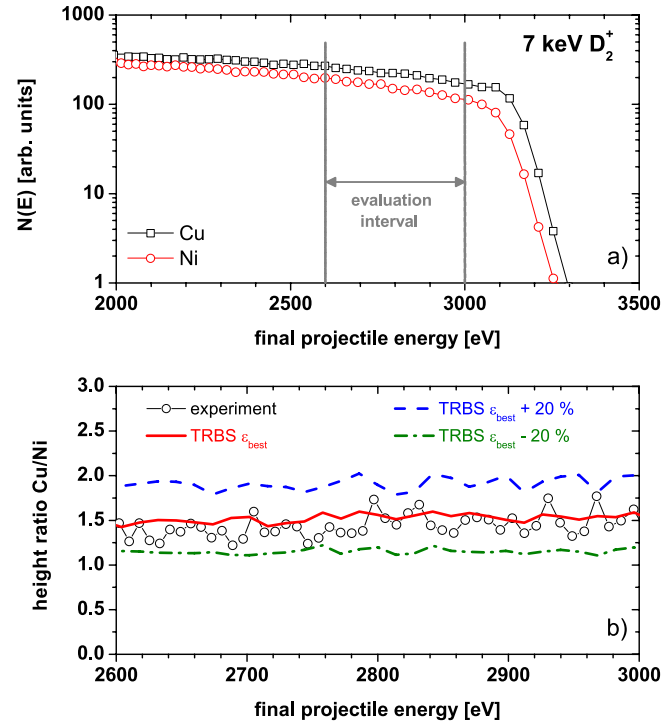

Fig. 4. (a) Experimental TOF-LEIS backscattering spectra of 7 keV D_2^+ ions measured on Cu and Ni samples. (b) Evaluation interval of the spectrum ratio Cu/Ni. Also shown are the results of TRBS simulations: as a red line—spectrum with optimized SCS of Ni $\varepsilon_{best} = 4.78 \times 10^{-15}$ eV cm^2/atom; as green dash-dotted and blue dashed lines—spectra for $\varepsilon_{best} \pm 20\%$. (For interpretation of the references to colour in this figure legend, the reader is referred to the web version of this article.)

deduced from the ratio of the spectrum heights N_{Ni}/N_{ref}, since N_{Ni}/N_{ref} comprises information on $[\varepsilon]_{ref}/[\varepsilon]_{Ni}$ (p. 47 in [45]); the electronic stopping cross section factor $[\varepsilon]$ takes into account electronic stopping on the way in and on the way out (p. 46 in [45]). In order to evaluate ε_{Ni}, the experimental ratios N_{Ni}/N_{ref} are compared to the results from corresponding TRBS simulations at energies close to the kinematic onset, where the shapes of the experimental spectra are perfectly reproduced by the simulations [37]. In the simulations, ε_{ref} is known [13] and ε_{Ni} is the only parameter to be optimized. Experimental spectra of 7 keV D_2^+ ions scattered from Cu (reference) and Ni as well as the experimental and simulated height ratios are shown in Fig. 4a and b, respectively. Dashed lines represent the energy window used in the evaluation. After convergence of the evaluation procedure (ε_{best}), simulation and experiment agree within 3%; two additional simulations, for which ε_{best} was varied by ± 20%, demonstrate how the height ratio is related to a variation of the SCS of Ni. In the evaluation of the spectrum heights, the evaluation interval is restricted to energies above half the primary energy, since at too low energies typical trajectories are almost entirely dominated by multiple scattering, i.e., by large impact parameter collisions, for which none of the screened potentials is sufficiently accurate. Whenever both approaches are applied to determine electronic stopping in backscattering geometry (evaluation of spectrum widths and spectrum heights, respectively), concordant results are obtained within experimental uncertainties, giving confidence in the evaluation methods.

5. Results and discussion

5.1. Target properties

When thin films are used to determine electronic stopping of slow ions in transmission and backscattering experiments, film thicknesses

have to be small (ultra-thin films with thicknesses < 20 nm). Therefore, properties such as surface purity, composition and roughness are important for stopping measurements. In transmission, film roughness can be estimated from the angular dependence of the energy loss (compare Section 4.2.1); in backscattering, information on film roughness can be deduced when the low energy edge in the energy spectrum is blurred (compared to the corresponding TRBS simulation). Note that in the present experiments the evaluation of energy spectra obtained for nanometer films did not reveal significant variations of the film thickness (compare Fig. 3). In the following, we want to discuss how surface and bulk contaminations affect the evaluation of the SCS in both experimental approaches.

When surface and bulk impurities are present in the self-supporting foils used in transmission measurements, ΔE as well as Δx must be corrected properly to extract the stopping power of the material of interest.

In backscattering measurements using thin metal films, the SCS is deduced from the width of the spectrum, ΔE_{RBS}, and the areal density obtained by RBS, $n_{metal}\Delta x$, via $\Delta E_{RBS} = [\varepsilon]\cdot n_{metal}\Delta x$ [45]. Low Z impurities in the thin film will increase the stopping power and lead to an increase of the spectrum width, while $n_{metal}\Delta x$ does not change. Consequently, evaluation of backscattering spectra obtained with thin metal films containing impurities will yield too high SCS values. The same is true for evaluation of the spectrum heights, since the presence of low Z impurities leads to a decrease of the plateau heights for the metal spectra [45].

In Fig. 5a, energy spectra of two ex-situ Ni films prepared in Linz are shown; the spectra were recorded using 8 keV D_2^+ ions for the same primary charge. Note that the plateau heights of both spectra do not coincide – in contrast to what one would expect for two films of the same material. Furthermore, the narrower spectrum corresponds to the film with larger thickness according to RBS. These observations are explained by a difference in the SCS of both films due to different concentrations of light impurities. According to XPS, all Ni films prepared ex-situ for this study contain a considerable amount of low Z impurities, mainly carbon, oxygen and, to a lesser extent, nitrogen. The concentrations of Ni atoms range from 75% to 86%, depending on vacuum conditions. Even if XPS is only semi-quantitative and not sensitive to hydrogen, its main advantage is that it provides information on the chemical state of the atomic species in the sample. The XPS analysis of our targets revealed only metallic nickel. The presence of impurities in Ni films when prepared ex-situ in high-vacuum setups may be generalized, since any reactive metal film, when prepared in a similar way, will be prone to incorporation of low Z impurities. So, careful characterization of the film contamination (H, C, N, O) is mandatory prior to any stopping measurements on reactive materials.

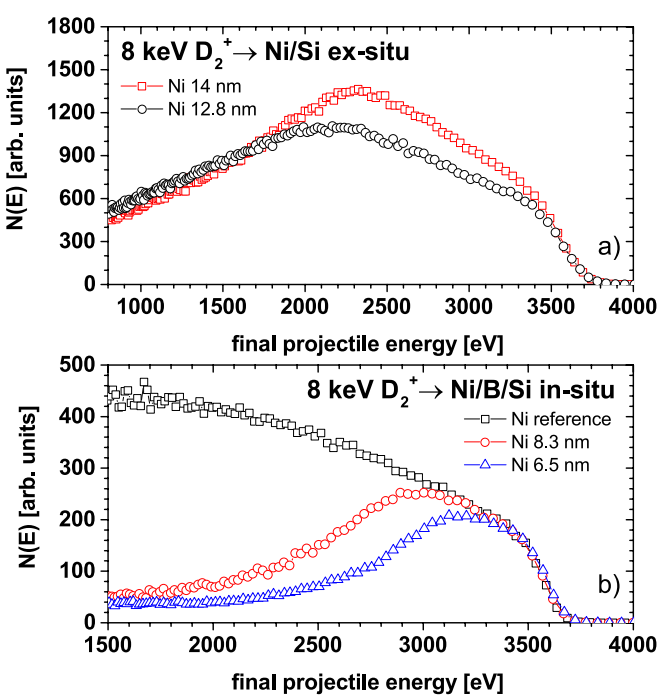

Fig. 5. (a) Experimental TOF-LEIS backscattering spectra of 8 keV D_2^+ ions measured on ex-situ prepared Ni films deposited on Si. (b) Experimental TOF-LEIS backscattering spectra of 8 keV D_2^+ ions measured on in-situ prepared Ni films of different thickness deposited on B/Si substrates. The reference corresponds to a clean Ni sheet.

Energy spectra of two ultra-thin Ni films (6.5 nm and 8.3 nm), prepared in-situ in UHV, and of a thick high purity Ni sheet after surface cleaning are shown in Fig. 5b (using 8 keV D_2^+ and data acquisition for the same primary charge). In contrast to Fig. 5a, the plateau heights of all three spectra coincide within 5% at energies close to the high energy onset, and the widths of the spectra reflect the thicknesses as determined by RBS. Consistently, AES measurements did not indicate any impurities. From these findings, we conclude that these Ni films prepared in-situ under UHV conditions are sufficiently pure so that the stopping power measurements are not affected by target impurities. Note that a possible hydrogen content in the samples cannot be excluded a priori. For the Ni sheet, the hydrogen content is limited to < 1% (atomic concentration) as deduced from TOF-ERD measurements. Obviously, also in the in-situ prepared nm-film the hydrogen content is sufficiently low so that it does not influence the results noticeably.

5.2. Electronic stopping in transmission and backscattering

In Fig. 6, the electronic stopping cross sections of Ni for H^+ and D^+ ions obtained by transmission measurements in Bariloche (BRC) and by backscattering experiments in Linz (LNZ), respectively, are displayed as function of the ion velocity in atomic units v/v_0, where v_0 denotes the Bohr velocity $v_0 = c/137$. Data obtained by use of ex-situ films in transmission and backscattering experiments coincide within experimental uncertainty. Note that this coincidence is just fortuitous, since cross check RBS and TOF-LEIS experiments on samples prepared in Bariloche and transmission measurements using foils produced in Linz did not yield concordant results. Backscattering measurements performed in UHV using in-situ prepared ultra-thin Ni films and thick high-purity Ni sheets yield concordant SCS data within experimental

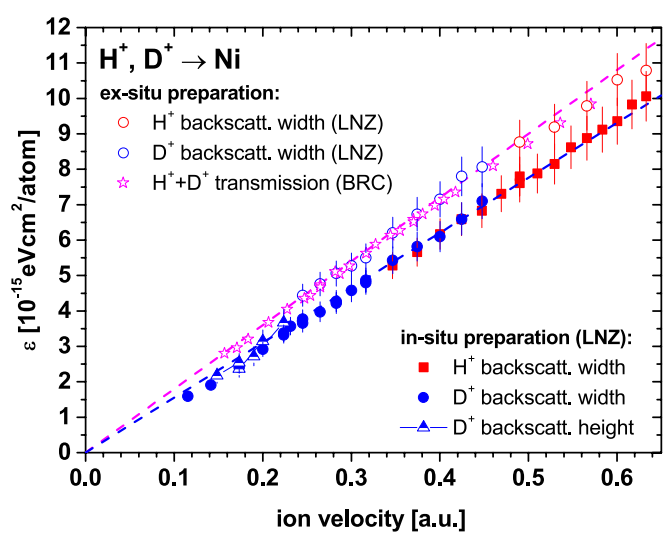

Fig. 6. Electronic stopping cross section of H^+ and D^+ ions in Ni as a function of the ion velocity. Open symbols: experimental results from samples prepared ex-situ. Full and half-full symbols: experimental results from samples prepared in-situ under ultra-high-vacuum conditions.

uncertainties (standard deviation: ± 7% and ± 10% for velocities $v < 0.2$ a.u., respectively). These results are lower by ~15% than those obtained by use of ex-situ prepared samples.

One may try to correct the SCS data deduced from measurements employing the ex-situ samples for contributions of bulk impurities (C, O) following Bragg's rule [46]:

In case of transmission experiments, the stopping power of Ni can be obtained by computing $S_{Ni} = [\Delta E_{total} - S_C \cdot \Delta x_C - S_O \cdot \Delta x_O]/\Delta x_{Ni}$; where ΔE_{total} is the energy loss measured for the contaminated foil. The stopping power values for carbon (S_C) and oxygen (S_O) are from TRIM tables [34]. The effective foil thickness is measured by XRR, resulting in 15 nm ± 10% (standard deviation), and independently by AFM, resulting in 19 nm ± 10%. The relative concentrations in bulk and surface of the components are obtained from the XPS depth profiles. As a result, the "15 nm foil" consists of impurity rich surface layers (thickness ~2 nm, atomic concentrations 25% Ni, 55% C, and 20% O), with a Ni rich layer inbetween (thickness 15 ± 1 nm, atomic concentrations 75% Ni, 5% O, and 20% C). Thus, the seeming discrepancy between the thickness values measured by the XRR and by AFM is resolved.

From the concentration profiles obtained by XPS, effective thicknesses of $\Delta x_{Ni} = 11.25$ nm, $\Delta x_C = 6$ nm, and $\Delta x_O = 1.75$ nm are deduced.

For backscattering measurements, the SCS of Ni can be extracted from the experimentally deduced SCS, ε_{expt}, via $\varepsilon_{expt} \cdot N_{expt} \Delta x = \varepsilon_{Ni} \cdot N_{Ni} \Delta x + \varepsilon_O \cdot N_O \Delta x + \varepsilon_C \cdot N_C \Delta x$. In the RBS thickness evaluation only the Ni atoms are considered, i.e., $\varepsilon_{expt} \cdot N_{expt} \Delta x = \varepsilon_{expt} \cdot N_{Ni} \Delta x$. Thus, the SCS of Ni can be obtained by a correction of the experimental results via $\varepsilon_{Ni} = \varepsilon_{expt} - \varepsilon_O\, c_O - \varepsilon_C\, c_C$, where $c_O = N_O/N_{Ni}$ and $c_C = N_C/N_{Ni}$ are relative atomic concentrations as deduced by XPS. Note that this procedure represents a simplified version of Bragg's Rule, since it does not consider any hydrogen impurities and it ignores the contribution of the impurities to multiple scattering. A recent study showed that latter assumption is sufficiently correct for protons [47]. Similarly, as for the data obtained in transmission, values for the SCS of oxygen and carbon, ε_O and ε_C, are taken from TRIM [34]. According to XPS, the relative impurity concentrations for O and C in the ex-situ sample, from which the results shown in Fig. 6 were obtained, result in $c_O = 0.114$ and $c_C = 0.023$, respectively, equivalent to atomic concentrations of 88% Ni, 10% C and 2% O.

In Fig. 7, we present the velocity dependent electronic stopping cross section of Ni for hydrogen ions (H^+, H_2^+, D^+ and D_2^+) employing in-situ prepared Ni samples (backscattering), and targets produced ex-situ (transmission and backscattering), for which the SCS data have been corrected for the presence of low Z contaminations. In backscattering, the impurity correction of the data for the ex-situ samples leads to perfect agreement with the results for the in-situ targets. For the data measured in transmission, the impurity correction reduces the discrepancy considerably, so that the final transmission data exceed the results from backscattering by less than ~10%.

From the discussion of the possible systematic errors in thickness and composition of the targets used, we are convinced that the in-situ prepared targets (Ni sheet and nm-film) are the most appropriate samples for SCS measurements. The fact that not for all ex-situ targets the corrected SCS data coincide with the in-situ data can be explained by possible inherent uncertainties in the XPS results and the characterization of the foils used. The fact that the corrected backscattering data agree well with the data for the high purity samples means that either both impurity concentrations and TRIM stopping are correct or their systematic errors compensate.

Also shown are experimental SCS data from literature (Möller et al. [48] and Arkhipov et al. [49]) and the SCS values of SRIM-2013 [50] (black dash-dotted line), respectively. The data of Möller et al. are higher than the in-situ measurements (e.g., at $v = 0.35$ a.u. about 10%) and coincide with the corrected results obtained for ex-situ samples in transmission geometry, whereas the data of Arkhipov et al. exhibit considerably higher SCS values (by ~50% w.r.t. in-situ results at

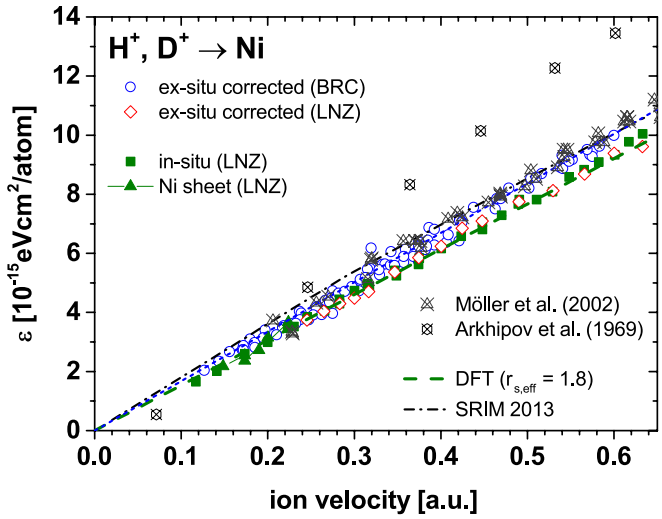

Fig. 7. Electronic stopping cross section of H^+, H_2^+, D^+ and D_2^+ ions in Ni as a function of the ion velocity. Open symbols and half-full symbols: corrected values of the experimental results obtained from samples prepared ex-situ. Full symbols: resulting SCS from samples prepared in-situ under ultra-high-vacuum conditions. Crossed symbols: SCS data from literature [48,49]. Black dash-dotted line: SCS of Ni from SRIM-2013 [50]. Dashed green line indicates DFT result [26] for a FEG of effective density $r_{s,eff} = 1.8$ (corresponding to the experimental plasmon energy [51]).

$v = 0.35$ a.u.). For obvious reasons, the SRIM data cannot be expected to be more precise than the underlying experimental data. Thus, the fact that the SRIM data are too high may be a consequence of the presence of impurities in the targets used in previous experiments and demonstrates the importance of target characterization in stopping measurements.

The SCS of Ni is proportional to the ion velocity, similarly as for a FEG material (e.g., Al [16,17]). Furthermore, the slope of the experimental in-situ SCS data is described perfectly by the DFT-model [26] for $r_{s,eff} = 1.8$ (corresponding to the plasmon energy $\hbar\omega_{p,Ni} = 19.5$ eV [51]), similarly as observed for Pt [14].

Finally, we want to address the point of possibly different impact parameter regimes being relevant in experiments performed in transmission and in backscattering geometry. In the single scattering regime, i.e., at high ion energies, in both experimental geometries only distant collisions contribute to electronic stopping along the trajectories. In backscattering there will be only one close collision with enhanced electronic losses, by which the backscattering spectrum will be displaced. In contrast, at very low ion energies multiple scattering will lead to a broadening of the impact parameter spectrum, but different in transmission and in backscattering geometry [27]. In transmission, smaller electronic stopping is expected due to less contribution from collisions at smaller impact parameters (higher electron densities). In contrast, the final data obtained in transmission geometry exhibit SCS that are higher than those obtained in backscattering (see Fig. 7). The reason for this observation most probably is related to the quantification of impurities, which is not accurate enough to allow for a conclusion concerning a possibly different impact parameter selection in transmission and in backscattering experiments at the very low proton velocities considered here.

6. Conclusions

We determined the electronic stopping cross section of Ni for hydrogen ions (H^+, H_2^+, D^+ and D_2^+) ions in transmission and backscattering experiments using samples prepared in different experimental setups: foils and films produced ex-situ in high-vacuum chambers, a Ni sheet and nm-films prepared in-situ in a UHV chamber.

The ex-situ prepared samples exhibit systematically higher SCS with respect to the in-situ prepared ones. This difference was attributed to contaminations in the ex-situ prepared samples. In the present experiments, the discrepancy was lower than 15%, even for 20% to 30% of low Z impurities. When corrected for impurities by Bragg's Rule, the difference between ex-situ and in-situ data is reduced to < 10%. Inaccuracies in the target characterization, i.e., thickness, impurity concentrations and accuracy of the TRIM data, may be responsible for this remaining discrepancy. Therefore, highest precision is expected for reactive target materials when sample preparation is carried out in-situ. If the experimental setups do not allow in-situ sample preparation under UHV conditions, a thorough characterization of ultra-thin foils and films has to be performed to minimize systematic errors.

Acknowledgements

Financial support of this work by the FWF (FWF-Project P22587-N20 and FWF-Project P25704-N20), the OEAD (OEAD Project AR01/2013), UNCuyo (06/C478, 06/C517), CONICET (PIP 112 201101 00594) and ANPCYT (AU/12/03, PICT 2012-0124) are gratefully acknowledged. We are grateful to Daniel Primetzhofer for the TOF-ERD analysis of the Ni sheet.

References

[1] L. Moroz, G. Baratta, G. Strazulla, L. Starukhina, E. Dotto, M.A. Barucci, G. Arnold, E. Distefano, Icarus 170 (2004) 214–228.
[2] B.M. Berger, R. Stadlmayr, G. Meisl, M. Čekada, C. Eisenmenger-Sittner, T. Schwarz-Selinger, F. Aumayr, Nucl. Instr. Meth. B 382 (2016) 82–85.
[3] S. Lazanu, A. Slav, A.-M. Lepadatu, I. Stavarache, C. Palade, G. Iordache, M.L. Ciurea, Appl. Phys. Lett. 101 (2012) 242106.
[4] D. Kriegner, J. Furthmüller, R. Kirchschlager, J. Endres, L. Horak, R. Cejpek, H. Reichlova, X. Marti, D. Primetzhofer, A. Ney, G. Bauer, F. Bechstedt, V. Holy, G. Springholz, Phys. Rev. B 94 (2016) 054112.
[5] C.P. Race, D.R. Mason, M.W. Finnis, W.M.C. Foulkes, A.P. Horsfield, A.P. Sutton, Rep. Prog. Phys 73 (2010) 116501.
[6] P. Sigmund, Particle Penetration and Radiation Effects – General Aspects and Stopping of Swift Point Charges, Springer Verlag, Berlin-Heidelberg, 2006.
[7] P. Sigmund, A. Schinner, Eur. Phys. J. D 68 (2014) 318.
[8] J.F. Ziegler, J. Appl. Phys. 85 (1999) 1249.
[9] N.R. Arista, A.F. Lifschitz, Advances in Quantum Chemistry, 2004, pp. 47–77 Part 1.
[10] M.A. Zeb, J. Kohanoff, D. Sánchez-Portal, A. Arnau, J.I. Juaristi, E. Artacho, Phys. Rev. Lett. 108 (2012) 225504.
[11] E.E. Quashie, B.C. Saha, A.A. Correa, Phys. Rev. B 94 (2016) 155403.
[12] V.U. Nazarov, J.M. Pitarke, Y. Takada, G. Vignale, Y.-C. Chang, Phys. Rev. B 76 (2007) 205103.
[13] S.N. Markin, D. Primetzhofer, M. Spitz, P. Bauer, Phys. Rev. B 80 (2009) 205105.
[14] E.D. Cantero, G.H. Lantschner, J.C. Eckardt, N.R. Arista, Phys. Rev. **A** 80 (2009) 032904.
[15] D. Goebl, D. Roth, P. Bauer, Phys. Rev. A 87 (2013) 062903.
[16] J.E. Valdés, G. Martínez Tamayo, G.H. Lantschner, J.C. Eckardt, N.R. Arista, Nucl. Instr. Meth. B 73 (1993) 313–318.
[17] D. Primetzhofer, S. Rund, D. Roth, D. Goebl, P. Bauer, Phys. Rev. Lett. 107 (2011) 163201.
[18] E.A. Figueroa, E.D. Cantero, J.C. Eckardt, G.H. Lantschner, J.E. Valdés, N.R. Arista, Phys. Rev. A 75 (2007) 010901.
[19] P. Sigmund, A. Schinner, Nucl. Instr. Meth. B 410 (2017) 78–87.
[20] P. Mertens, P. Bauer, D. Semrad, Nucl. Instr. Meth. B 15 (1986) 91–95.
[21] J.B. Staunton, A. Marmodoro, A. Ernst, J. Phys. Cond. Matter 26 (2014) 274210.
[22] E. Fermi, E. Teller, Phys. Rev 72 (1947) 399–408.
[23] P.M. Echenique, R.M. Nieminen, R.H. Ritchie, Solid State Commun. 37 (1981) 779.
[24] M.J. Puska, R.M. Nieminen, Phys. Rev. B 27 (1983) 6121.
[25] A. Mann, W. Brandt, Phys. Rev. B 24 (1981) 4999–5003.
[26] J.I. Juaristi, M. Alducin, R. Díez Muiño, H.F. Busnengo, A. Salin, Phys. Rev. Lett. 100 (2008) 116102.
[27] D. Goebl, K. Khalal-Kouache, D. Roth, E. Steinbauer, P. Bauer, Phys. Rev. A 88 (2013) 032901.
[28] C. Celedón, E.A. Sánchez, M.S. Moreno, N.R. Arista, J.D. Uribe, M. Mery, J.E. Valdés, P. Vargas, Phys. Rev. A 88 (2013) 012903.
[29] W. Möller, G. Pospiech, G. Schrieder, Nucl. Instr. Meth. 130 (1975) 265.
[30] M. Famá, J.C. Eckardt, G.H. Lantschner, N.R. Arista, Phys. Rev. A 62 (2000) 062901.
[31] G. Molière, Z. Naturforschung, vol. 2a (1947) 133–145.
[32] C.E. Celedón, E.A. Sánchez, L. Salazar Alarcón, J. Guimpel, A. Cortés, P. Vargas, N.R. Arista, Nucl. Instr. Meth. B 360 (2015) 103–110.
[33] J.P. Biersack, E. Steinbauer, P. Bauer, Nucl. Instr. Meth. B 61 (1991) 77–82.
[34] J.F. Ziegler, J.P. Biersack, U. Littmark, The Stopping and Range of Ions in Solids, Pergamon Press, New York, 1985.
[35] D.J. O'Connor, J.P. Biersack, Nucl. Instr. Meth. B 15 (1986) 14–19.
[36] D. Primetzhofer, S.N. Markin, D.V. Efrosinin, E. Steinbauer, R. Andrzejewski, P. Bauer, Nucl. Instr. Meth. B 269 (2011) 1292–1295.
[37] D. Roth, D. Goebl, D. Primetzhofer, P. Bauer, Nucl. Instr. Meth. B 317 (2013) 61–65.
[38] Colutron Research Corporation, Boulder, Colorado, USA, http://www.colutron.com.
[39] P. Sigmund, K. Winterbon, Nucl. Instr. Meth. 119 (1974) 541.
[40] W. Eckstein, Computer Simulations of Ion-Solid Interactions, Springer-Verlag, Berlin, 1991.
[41] M. Nastasi, J.W. Mayer, J.K. Hirvonen, Ion-Solid Interactions: Fundamentals and Applications, Cambridge University Press, 1996.
[42] J. Lindhard, V. Nielson, M. Scharff, Mat. Fys. Medd. Dan. Vid. Selsk. 36 (1968) 10.
[43] M. Famá, G.H. Lantschner, J.C. Eckardt, C.D. Denton, N.R. Arista, Nucl. Instr. Meth. B 164 (2000) 241.
[44] M. Draxler, S.N. Markin, S.N. Ermolov, K. Schmid, C. Hesch, R. Gruber, A. Poschacher, M. Bergsmann, P. Bauer, Vacuum 73 (2004) 39–45.
[45] J.R. Tesmer, M.A. Nastasi (Eds.), Handbook of Modern Ion Beam Analysis, Materials Research Society, Pittsburgh, 1995.
[46] W.H. Bragg, R. Kleeman, Philos. Mag. 10 (1905) 318.
[47] B. Bruckner, D. Roth, D. Goebl, P. Bauer, D. Primetzhofer, Nucl. Instr. Meth. B 423 (2018) 82.
[48] S.P. Möller, A. Csete, T. Ichioka, H. Knudsen, U.I. Uggerhoj, H.H. Andersen, Phys. Rev. Lett. 88 (2002) 193201.
[49] E.P. Arkhipov, Yu.V. Gott, Sov. Phys.-JETP 29 (1969) 615.
[50] J.F. Ziegler, J.P. Biersack, M.D. Ziegler, SRIM, the Stopping and Range of Ions in Matter, SRIM Company, 2008.
[51] H.A.E. Hagelin-Weaver, J.F. Weaver, G.B. Hoflund, G.N. Salaita, J. Alloys Compd. 389 (2005) 34–41.